JOURNAL OF PROPULSION AND POWER
Vol. 28, No. 1, January–February 2012

Simulation of Hypersonic Shock/Turbulent Boundary-Layer Interactions Using Shock-Unsteadiness Model

Amjad A. Pasha* and Krishnendu Sinha†
Indian Institute of Technology Bombay, Mumbai 400076, India

DOI: 10.2514/1.B34191

In hypersonic flows, the interaction of a shock wave with a turbulent boundary layer can result in flow separation and high aerothermal loads. In this paper, cone–flare configurations with different flare angles and freestream Mach numbers are simulated using Reynolds-averaged Navier–Stokes method, and results are compared with experimental data. The standard Spalart–Allmaras and k-ω turbulence models do not predict flow separation at the cone–flare junction, and therefore yield a large deviation from the surface pressure measurements. Sinha et al. ("Modeling Shock-Unsteadiness in Shock/Turbulence Interaction," *Physics of Fluids*, Vol. 15, No. 8, 2003, pp. 2290–2297) proposed a shock-unsteadiness model to account for the effect of unsteady shock motion in a steady mean flow. The shock-unsteadiness correction damps turbulence amplification at the shock and results in significant improvement in predicting flow separation and reattachment. The flow topology in the interaction region, in terms of the pattern of shocks and expansion waves, is predicted correctly by the modified turbulence models. The resulting surface pressure distribution matches experimental data well.

Nomenclature

b_1'	=	shock-unsteadiness damping parameter
C_f	=	skin-friction coefficient
c_{b_1}'	=	shock-unsteadiness parameter
f_s	=	shock-identifying function
k	=	turbulent kinetic energy
M_{1n}	=	upstream Mach number normal to shock
P_k	=	production of turbulent kinetic energy
s	=	arc length measured from cone–flare junction
S_{ii}	=	mean dilatation
S_{ij}	=	mean strain rate tensor
U	=	mean velocity in the streamwise direction
$\tilde{u}_i$	=	ith component of the mean velocity
y_2^+	=	wall-normal distance to nearest point in wall coordinates
δ_0	=	boundary-layer thickness upstream of interaction
ζ	=	dimensionless mean strain rate
μ_T	=	eddy viscosity
ν	=	kinematic molecular viscosity
$\tilde{\nu}$	=	modified turbulent kinematic viscosity
ω	=	turbulent specific dissipation rate

Subscripts

n	=	normal to shock wave
w	=	wall condition
∞	=	freestream condition

I. Introduction

INTERACTION of a turbulent boundary layer with shock waves is common in hypersonic flight: for example, on control surfaces, wing–body junctions, and airbreathing inlets. The potential of flow separation and localized high-pressure and high heat flux in the interaction region makes it imperative to predict it accurately. Several experimental and computational efforts have been directed toward this goal. Commonly studied configurations include compression corners [1], cylinder flares [2], shock waves impinging on flat plate boundary layers [3], and single or double fins on plates [4].

Engineering prediction of shock wave/turbulent boundary-layer interaction relies on Reynolds-averaged Navier–Stokes (RANS) simulations. However, conventional turbulence models have significant disagreement with experimental data, especially in the presence of strong shock waves [5,6]. For example, the size of the separation region and the surface pressure are not predicted correctly. Several modifications have been proposed to improve predictions, such as compressibility correction, length-scale modification, and rapid compression correction [2,5]. The outcomes of these modifications vary from one test case to other.

In a shock wave/turbulent boundary-layer interaction, the shock wave oscillates about its mean position in response to the unsteady turbulent fluctuations passing through it. The scale of turbulent motion is a function of the boundary-layer conditions, like Reynolds number, which in turn is expected to influence the scale of shock motion. Turbulence models used in RANS treat the shock wave as steady, and they do not account for the unsteady motion of the shock. This has been pointed out as one of the major limitations of existing turbulence models [5,7].

Sinha et al. [8] studied the effect of shock unsteadiness on turbulence amplification across a shock wave. An additional source term was identified in the turbulent kinetic energy (TKE) equation that was proportional to the correlation of the shock speed and the streamwise velocity fluctuations. An in-phase coupling of the unsteady shock motion with the upstream turbulent fluctuations was found to have a damping effect on TKE amplification. A model for the shock-unsteadiness effect was developed based on results from the linear interaction analysis of Mahesh et al. [9]. The new model matches direct numerical simulation data for the evolution of TKE, when a homogeneous isotropic turbulence field interacts with a normal shock. By comparison, standard models like k-ϵ and k-ω, which neglect the shock-unsteadiness damping effect, overly amplify the TKE across a shock wave.

Sinha et al. [10] applied the shock-unsteadiness modification to commonly used one- and two-equation turbulence models like the k-ϵ, k-ω, and Spalart–Allmaras models. The implementation is such that the correction is applied only in regions of strong compression, leaving the original model unchanged otherwise. In supersonic compression corner flows [10], the shock-unsteadiness model reduces the amplification of TKE at the separation shock. A lower turbulence level enhances flow separation, such that the separation

Received 28 November 2010; revision received 30 May 2011; accepted for publication 18 June 2011.

*Doctoral Student, Department of Aerospace Engineering.

†Associate Professor, Department of Aerospace Engineering. Senior Member AIAA.

location moves upstream to match experimental measurement. In case of oblique shock impinging on a turbulent boundary layer [11], the shock-unsteadiness model shows similar improvement. The size of the separation bubble and the wall pressure distribution match experimental data better than the standard model. The location of the separation shock, its interaction with the incident shock wave, and the resulting pattern of shocks and expansion waves match the experimental schlieren image closely.

The majority of research on shock/turbulent boundary-layer interaction is in the supersonic regime. At hypersonic Mach numbers, the shock waves generated by flow deflection are much stronger than those at supersonic speeds. Therefore, the shock/boundary-layer interactions observed in hypersonic flows are usually stronger, resulting in a larger separation bubble and higher peak pressure than the supersonic ones. Furthermore, hypersonic flows are often characterized by multiple shock waves interacting with each other. These shock–shock interactions generate additional compression and expansion waves, and free shear layers. Simulating all the flow features and the underlying flow physics makes it harder to predict hypersonic shock/boundary-layer interactions than their supersonic counterparts.

In this paper, we study hypersonic shock/boundary-layer interaction on cone–flare configurations. A naturally developing turbulent boundary layer on a long cone with a small cone angle interacts with the oblique shock generated at the cone–flare junction. Tests were conducted with different flare angles at varying freestream conditions [12]. The resulting experimental data set spans a range of shock/boundary-layer interactions, from weak ones with no flow separation at the corner to strong interactions with a large separation bubble at the cone–flare junction. RANS simulations using conventional turbulence models suppress flow separation, and therefore do not reproduce the correct shock structure in the interaction region. Surface pressure data are a good indicator of the flow topology, and a large discrepancy is found between the computed surface pressure and the experimental measurements. The objective of the current work is to apply the shock-unsteadiness modification of Sinha et al. [8] to these hypersonic shock/boundary-layer interactions flows. Based on past experience, the shock-unsteadiness correction is expected to enhance flow separation at the cone–flare junction. This will result in a better matching of the flow topology and the shock structure in the interaction region with those observed in the experiments. The paper describes the implementation of the shock-unsteadiness correction in hypersonic configurations and evaluates its efficacy in predicting the correct separation location.

The experimental test cases are presented in the next section, and the simulation methodology is described subsequently. The shock-unsteadiness correction to one- and two-equation turbulence models, as proposed in [10], is summarized for completeness. The numerical algorithm and computational grid used in the simulation are outlined briefly, and it is followed by a detailed grid refinement study. Next, solutions computed for the experimental test cases using the standard and modified turbulence models are discussed. A detailed description of the mean flowfield and a comparison of the computed surface data to the experimental measurements are presented for each case. A similar study is presented in [13], which differs from the current work in terms of the cone–flare geometry. The earlier paper uses flare angles measured with respect to the geometric axis. In the current work, the flare angles are taken with reference to the cone surface. This is based on the correction reported by Roy and Blottner [1].

II. Test Case

The configuration studied by Holden [12] is a 2.66-m-long cone with a 6° half-cone angle and a flare of length 0.23 m (see Fig. 1). Two flare angles were considered, and the models were tested in the Calspan 96 in. shock tunnel. The flare angle is measured with reference to the cone surface, and the cone–flare junction is placed at $x = 0$. Thus, negative values of x correspond to the cone surface and the flare has positive x values. A constant pressure boundary layer develops over the cone, undergoes natural transition, and then interacts with the oblique shock generated at the cone–flare junction. Flow prediction in the shock/boundary-layer interaction region, identified in Fig. 1, is the primary focus of this work.

Models with two flare angles, 30 and 36°, were tested at two Mach numbers (nominally, 11 and 13), resulting in four test cases. The freestream and geometric parameters for different cases are listed in Table 1. A constant wall temperature of 294.44 K is taken along the cone–flare surface for all the cases. The resulting T_w/T_{aw} values for each case are also listed in the table. Note that a recovery factor of 0.89 is used to compute the adiabatic wall temperature. Air is used as the test gas in these runs, and perfect gas assumption is applicable owing to low stagnation enthalpy.

A single-pass schlieren system was used for flow visualization. Static pressure was measured along the model using piezoelectric pressure transducers, and platinum thin-film gauges were used to obtain the heat transfer rate on the surface. The uncertainties associated with the pressure and heating rate data were estimated to be $\pm 3\%$ and $\pm 5\%$, respectively. Surface pressure data are a good indicator of the separation point and have a one-to-one correspondence with the shock structure observed in the schlieren images. The majority of the comparisons between numerical simulations and experimental data are therefore based on the pressure measurements. A limited comparison with surface heat-flux data is also presented.

III. Simulation Methodology

We solve the axisymmetric form of the RANS equations [14] for the mean flow. The one-equation Spalart–Allmaras model [15] and the two-equation k-ω model of Wilcox [16] are used for turbulence closure. The Spalart–Allmaras model solves a transport equation for $\tilde{\nu}$, which is identical to the kinematic eddy viscosity ν_T, except in the viscous sublayer and the buffer region close to a solid boundary. The k-ω turbulence model solves transport equations for the TKE k and the specific dissipation rate ω. The turbulence models do not include any compressibility corrections. This is because traditional compressibility corrections in the form of dilatation dissipation and the pressure dilatation terms distort the incoming boundary layer and predict low values of skin friction compared with experiments upstream of the interaction region [17].

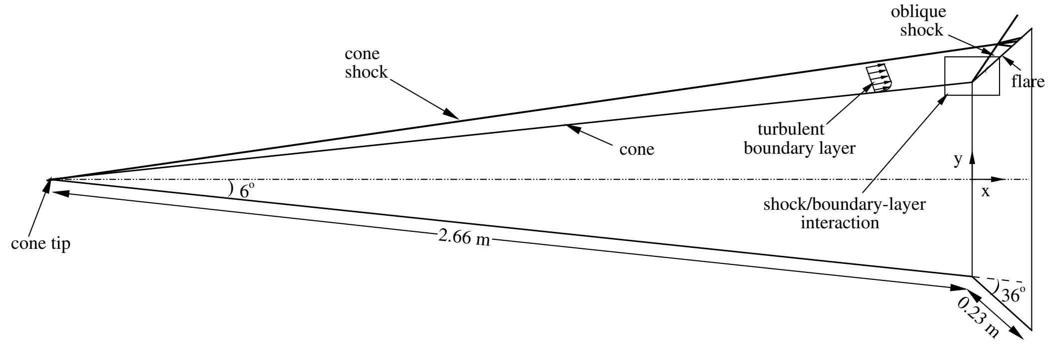

Fig. 1 Geometric configuration with flow schematic for the hypersonic shock wave/ turbulent boundary-layer interaction test cases of Holden [12].

Table 1 Freestream conditions and flare angles for hypersonic cone–flare configurations

	Test cases			
	1	2	3	4
Cone–flare angle, °	36	36	30	30
Freestream Mach number M_∞	13.1	10.97	12.92	10.98
Freestream temperature T_∞, K	57.0	65.4	60.9	67.4
Freestream pressure P_∞, kPa	0.51	0.62	0.5	0.63
Unit Reynolds number $Re_{1\infty} \times 10^6$, m^{-1}	1.385	1.145	1.219	1.113
Wall temperature/adiabatic wall temperature T_w/T_{aw}	0.15	0.17	0.14	0.17
Stagnation enthalpy H_0, MJ/kg	2.0	1.6	2.1	1.7

The freestream values of the mean flow variables are as per the data presented in Table 1. For the k-ω turbulence model, freestream conditions of $\omega_\infty = 10U_\infty/L$ and $k_\infty = 0.01\nu_\infty\omega_\infty$ are used as per Menter's recommendation [18], where L is a characteristic length. The freestream boundary condition for the Spalart–Allmaras turbulence model is set to $\tilde{\nu}_\infty = 0.1\nu_\infty$. The surface of the cone–flare geometry is specified as a no-slip isothermal and zero normal pressure gradient boundary. The wall values of the turbulence quantities are set at $\tilde{\nu} = 0$, $k = 0$, and $\omega = 60\nu_w/\beta_1\triangle y_1^2$. Here, $\beta_1 = 3/40$ is a model constant and $\triangle y_1$ is the normal distance to the grid point nearest to the wall.

A. Shock-Unsteadiness Modification

The shock-unsteadiness model was first proposed by Sinha et al. [8] for homogeneous turbulence/normal shock interaction, and it was subsequently incorporated in one- and two-equation turbulence models applied to shock/boundary-layer interaction [10]. The simplicity of the shock-unsteadiness correction term and its basis in underlying physical phenomena makes it attractive to use in practical applications. The model is briefly discussed below, and more details can be found in the original references.

The production of TKE in the standard k-ω turbulence model is given by

$$P_k = \mu_T S^2 - \frac{2}{3}\bar{\rho}kS_{ii} \tag{1}$$

Here, $S_{ij} = \frac{1}{2}(\partial\tilde{u}_i/\partial x_j + \partial\tilde{u}_j/\partial x_i)$, the parameter $S^2 = 2S_{ij}S_{ji} - \frac{2}{3}S_{ii}^2$, and $\mu_T = \bar{\rho}k/\omega$. It can be shown that, in a shock wave, P_k is proportional to S_{ii}^2, which is very large in magnitude. This results in excessively high values of TKE behind the shock, which may be the reason why the standard k-ω model often predicts delayed separation in shock/boundary-layer interaction flows. Sinha et al. [8] argued that the eddy viscosity assumption breaks down in the highly nonequilibrium flow through a shock wave, and a more realistic amplification of k is obtained by setting $\mu_T = 0$ in the production term. This results in $P_k \propto S_{ii}$, and therefore a lower amplification of TKE than the original model.

As noted above, the shock motion caused by the upstream turbulent fluctuations results in a damping of TKE at the shock wave. Sinha et al. [8] studied this mechanism using linear theory and proposed the following model for the net production of TKE at the shock wave:

$$P_k = -\frac{2}{3}\bar{\rho}kS_{ii}(1 - b_1') \tag{2}$$

where the first term is obtained by setting $\mu_T = 0$ in Eq. (1), and the second term corresponds to the shock-unsteadiness damping mechanism. The parameter b_1' is used to model the correlation between the shock speed and streamwise velocity fluctuations:

$$b_1' = \max[0, 0.4(1 - e^{1-M_{1n}})] \tag{3}$$

It is zero for subsonic flows without shock waves, and it reaches an asymptotic value of 0.4 for high Mach numbers.

The shock-unsteadiness correction is applied in the k-ω framework by multiplying the eddy viscosity term in Eq. (1) by the factor

$$c_\mu' = 1 - f_s\left[1 + \frac{b_1'}{\sqrt{3}\zeta}\right], \quad \text{with} \quad f_s = \frac{1}{2} - \frac{1}{2}\tanh\left[5\left(\frac{S_{ii}\delta_0}{U_\infty}\right) + 3\right] \tag{4}$$

Here, $\zeta = S/\omega$ and f_s is an empirical function that locates the region of shock wave in terms of the mean dilatation S_{ii}. The functional form of f_s is identical to that used in [10], except for the fact that S_{ii} is normalized by U_∞/δ_0 instead of the local value of S. The quantity U_∞/δ_0 is found to be more robust than S in [11]. The characteristic length δ_0 and freestream velocity U_∞ are known a priori for a given simulation and can be specified as user input. The function f_s takes a value of 1 in shock and high-compression regions of the flowfield, such that $c_\mu' = -b_1'/\sqrt{3}\zeta$ and the modified production term in the k-ω model matches with that in Eq. (2). Otherwise, $f_s = 0$ and the standard form of the k-ω model is recovered.

Wilcox presents a k-ω stress-limiter model [3] that limits TKE production in a shock wave. The value of the limiter was set as $C_{\lim} = 7/8$ for the new k-ω model. In a normal shock, the stress-limiter model yields TKE production of the form

$$P_k = c\rho k|S_{ii}| \tag{5}$$

with $c = 1.15$. A value of $C_{\lim} = 1$ corresponds to the shear stress transport (SST) model [18] with $c = 1.09$. By comparison, the shock-unsteadiness correction yields a production term of the form given by Eq. (2) with $c = 2/3(1 - b_1')$. A lower (higher) value of b_1' results in a higher (lower) value of c, which in turn increases (decreases) TKE production and suppresses (enhances) flow separation. In the simulations presented below, the shock-unsteadiness parameter b_1' is around 0.3, which corresponds to $c \simeq 0.46$. A relatively higher value of c used in the new k-ω and SST models may therefore result in a smaller separation bubble compared with that obtained using the shock-unsteadiness correction.

In the Spalart–Allmaras model, the mean flow influences the turbulence field via the production term that is a function of the mean vorticity. The eddy viscosity is therefore insensitive to the mean dilatation in a shock wave. The mean vorticity field in a turbulent boundary layer changes across a shock wave. This can alter the production term, and thus can change $\tilde{\nu}$ in the vicinity of the shock. In a 24° compression corner flow at Mach 2.84, for example, the interaction of a turbulent boundary layer with an oblique shock results in a small increase in $\tilde{\nu}$ (less than 5% of the local $\tilde{\nu}$ value).

Interaction with a shock wave enhances the turbulent fluctuations in a flow. Sinha et al. [8] proposed the following model for the amplification of the TKE and the turbulent dissipation rate ϵ when homogeneous isotropic turbulence interacts with a shock wave:

$$\frac{k_2}{k_1} = \left(\frac{\tilde{u}_{n,1}}{\tilde{u}_{n,2}}\right)^{(2/3)(1-b_1')} \quad \text{and} \quad \frac{\epsilon_2}{\epsilon_1} = \left(\frac{\tilde{u}_{n,1}}{\tilde{u}_{n,2}}\right)^{(2/3)c_{\epsilon 1}'} \tag{6}$$

where b_1' is given by Eq. (3) and $c_{\epsilon 1}' = 1.25 + 0.2(M_{1n} - 1)$. The subscripts 1 and 2 refer to the locations upstream and downstream of the shock, respectively, and $\tilde{u}_n$ is the mean flow velocity normal to the shock. The kinematic eddy viscosity $\tilde{\nu} \propto k^2/\epsilon$, which yields

$$\frac{\tilde{\nu}_2}{\tilde{\nu}_1} = \left(\frac{k_2}{k_1}\right)^2 \frac{\epsilon_1}{\epsilon_2} = \left(\frac{\tilde{u}_{n,1}}{\tilde{u}_{n,2}}\right)^{c_{b_1}'} \tag{7}$$

This can be achieved by a source term of the form $-c_{b_1}'\bar{\rho}\,\tilde{\nu}\,S_{ii}$ in the transport equation for $\rho\tilde{\nu}$, where

$$c_{b_1}' = \frac{4}{3}(1 - b_1') - \frac{2}{3}c_{\epsilon 1}' \tag{8}$$

Note that this additional term is effective only in regions of strong dilatation, and therefore does not alter the standard Spalart–Allmaras model elsewhere.

The parameter c'_{b_1} can take either positive or negative values depending on the upstream Mach number. As per Eq. (7), the amplification of the eddy viscosity ν_T across a shock is given by the ratio of k^2 amplification to ϵ amplification. At supersonic Mach numbers, the amplification of k^2 is larger than that of ϵ, and therefore results in an increase in ν_T across the shock wave. This corresponds to a positive value of c'_{b_1} and a positive source term $-c'_{b_1}\bar{\rho}\,\tilde{\nu}\,S_{ii}$ in the model equation. A higher turbulence eddy viscosity results in reduction of the separation-bubble size in supersonic shock/boundary-layer interactions [10]. At hypersonic Mach numbers, the amplification of ϵ increases monotonically with M_{1n}, whereas k^2 amplification saturates for $M_{1n} > 1.8$. This results in a decrease of ν_T across a shock wave at hypersonic conditions. A lower value of ν_T increases the separation-bubble size in hypersonic shock/boundary-layer interaction, and it is opposite to that observed at supersonic Mach numbers.

B. Numerical Method and Computational Grid

The governing equations are discretized using a finite volume formulation, where the inviscid fluxes are computed using a modified low-dissipation form of the Steger–Warming flux-splitting approach [19]. The turbulence model equations are fully coupled to the mean flow equations. The details of the formulation are given by Sinha and Candler [20]. The method is second-order accurate both in streamwise and wall-normal directions. The viscous fluxes and the turbulent source terms are evaluated using a central difference method. The implicit data parallel line relaxation method of Wright et al. [21] is used to integrate the equations in time and reach a steady-state solution. The code has been used successfully in several supersonic and hypersonic applications [10,11,22].

The computational domain used in the simulations is shown in Fig. 2a. It spans the region between the cone tip and the end of flare in the wall-parallel i direction. In the wall-normal j direction, it extends from the cone–flare surface to the outer boundary, which is placed in the freestream flow outside the shock waves. The flow solution is insensitive to the actual location of the outer boundary as long as the shock wave generated by the cone–flare geometry does not intersect it. The inclination of the outer boundary is tailored such that the grid lines in the vicinity of the oblique shock generated by the cone tip are parallel to the shock wave. This eliminates any grid-induced distortion of the oblique shock along the length of the cone until it reaches the shock/boundary-layer interaction region.

A typical computation grid, shown in Fig. 2b, has about 600 points in the streamwise direction and 500 exponentially stretched points in the wall-normal direction. The grid points are clustered in the vicinity of the cone tip and at the cone–flare junction, such that there are about 300×375 points in the interaction region. The sensitivity of the solution to the computational grid is described below.

C. Grid Refinement Study

Flowfield solutions are computed using computational meshes with varying number of points in the wall-parallel and wall-normal directions. Also, the cell sizes in high-gradient regions, like shock waves, cone–flare junction, separation point, and reattachment location, are systematically varied to study their effect on the computed solution. A detailed grid convergence study of the 36° flare at Mach 13 using the shock-unsteadiness modified Spalart–Allmaras model is presented below. This is followed by a similar study for the shock-unsteadiness modified k-ω model. The computational solution obtained using the standard turbulence models is found to be less sensitive to the variation in computational grid than those obtained using the modified turbulence models.

For the baseline grid size of 600×500 points, the normal spacing adjacent to the wall is varied between 5×10^{-6} and 1×10^{-6} m, and the results computed using the modified Spalart–Allmaras model are presented in Fig. 3. The corresponding y_2^+ values range from 0.04 to 0.2 on the cone and from 1.4 to 7.6 on the flare. The surface pressure is mostly insensitive to the near-wall grid point distribution, except near the end of the computational domain. The variation in surface pressure in this region ($s \simeq 0.17$ m) is due to the impingement of the expansion fan generated by the shock–shock interaction outside the boundary layer. Refining the near-wall grid for a fixed number of grid points in the wall-normal direction results in a coarser mesh in the outer inviscid region. The consequent effect on the inviscid shock–shock interaction and the resulting surface pressure distribution can be seen in Fig. 3. The skin-friction coefficient, as expected, is more sensitive to the wall-normal spacing than the surface pressure, especially on the flare. There is about 2% variation between the two fine grids for $0.08\ \mathrm{m} < s < 0.18$ m. There is somewhat larger deviation further downstream, which is an effect of the outer inviscid interaction.

Next, the number of points in the wall-normal direction are varied and the results are presented in Fig. 4. Three exponentially stretched grids with 400, 500, and 600 grid points, with identical cell size adjacent to the wall, are used. This results in a stretching factor of

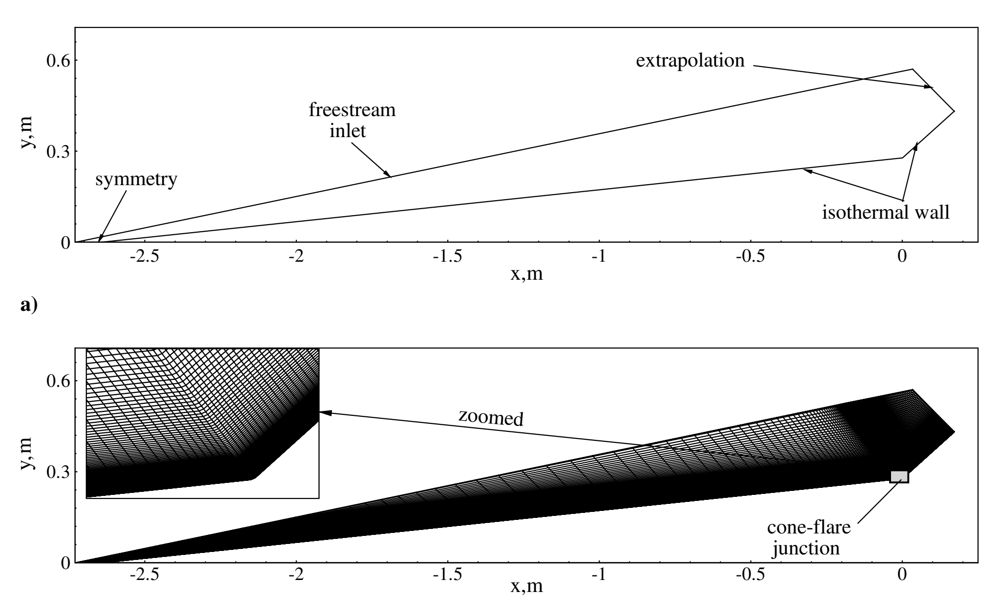

Fig. 2 2 Simulation of hypersonic cone-flare configuration: a) computational domain and boundary conditions, and b) typical computational mesh showing every third point in each direction. Inset shows a magnified view of the cone–flare junction.

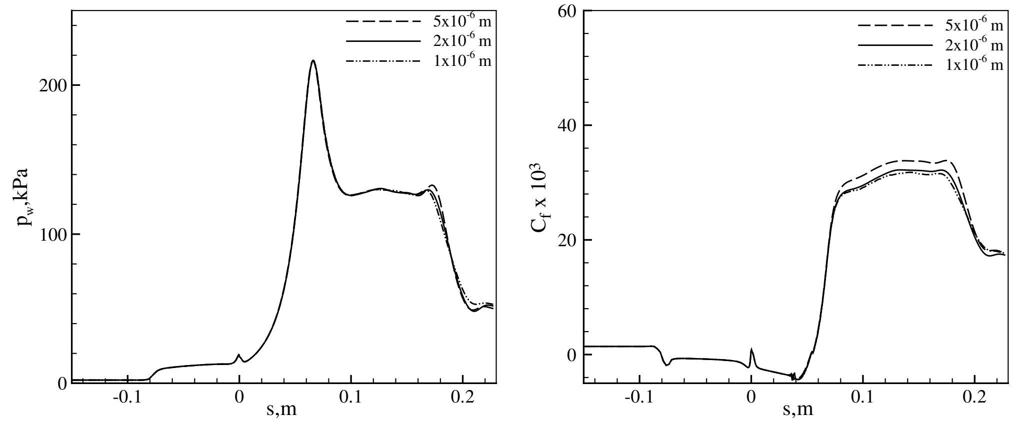

a) b)

Fig. 3 Effect of variation in wall-normal spacing on a) wall pressure and b) skin friction, using modified Spalart–Allmaras model for 36° flare at Mach 13.1.

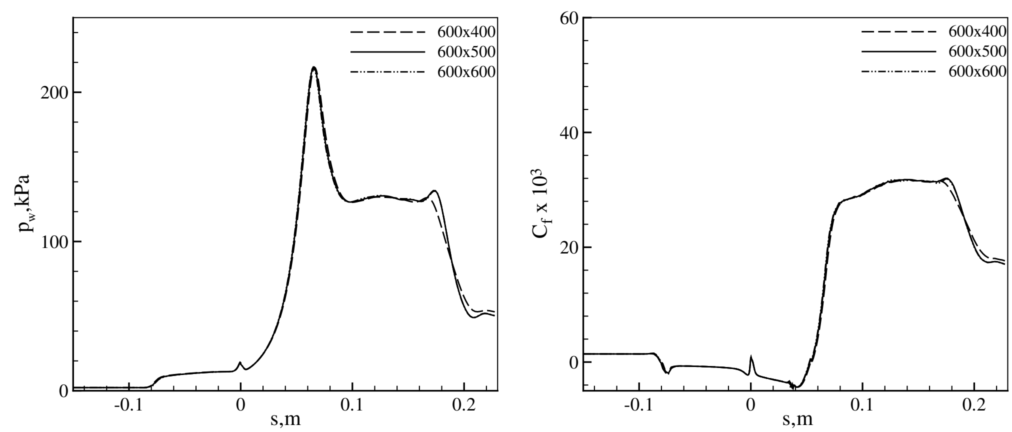

a) b)

Fig. 4 Effect of varying the number of wall-normal grid points on a) wall pressure and b) skin friction, using modified Spalart–Allmaras model for 36° flare at Mach 13.1.

1.023, 1.018, and 1.014, respectively, for the three grids. The majority of the variation is in the outer inviscid zone, and the near-wall grid is affected to a smaller extent. The surface data are almost identical over the entire geometry, except for the later part of the flare. This is once again caused by variation of the grid point density in the outer inviscid region, as explained above. The two finer grids yield overlapping results for the entire domain.

A similar procedure is followed in the wall-parallel direction by systematically varying the number of points along the wall. The surface properties are found to be less sensitive to the changes in the wall-parallel grid than that in the wall-normal direction, and 600 points are found to be adequate to obtain an accurate solution. Based on the above study, a computational mesh of 600×500 points with a wall-normal spacing of 2×10^{-6} m at the wall is chosen for computations using the standard and modified Spalart–Allmaras models. The corresponding y_2^+ value is about 0.08 on the cone and less than 3 on the flare.

The flowfield solution obtained using the k-ω model is more sensitive to the computational mesh than that of the Spalart–Allmaras model. The k-ω solution requires a substantially larger number of wall-parallel grid points (more than 1000) to attain grid independence. Even with finer grids, the changes in surface properties with successive refinement (presented in Figs. 5–7) are found to be appreciably higher than the corresponding Spalart–Allmaras model results. Furthermore, the k-ω computations are found to be prone to numerical instability, which restricts the time steps used in the simulation. The highest Courant–Friedrichs–Lewy (CFL) achievable for the k-ω model calculations (see Sec. IV) is significantly lower than those used for the Spalart–Allmaras computations.

The results obtained by varying the cell size adjacent to the wall and the number of grid points in the wall-normal and wall-parallel directions are presented next. Note that the pressure data computed using the modified k-ω model appear similar to that of the modified Spalart–Allmaras model, but the skin-friction coefficient has a local maximum near the reattachment point ($s \simeq 0.07$ m) that is not present in the modified Spalart–Allmaras model solutions.

The variation of skin-friction coefficient (Fig. 5b), when the wall-normal spacing at the wall is decreased from 2×10^{-6} to 0.5×10^{-6} m, shows a converging trend. The maximum deviation between the two finer grid predictions is 3%. The separation point located at $s = -0.085$ m changes by a small amount (0.005 m) for the three grids. The pressure data (Fig. 5a) show a similar trend, with the location of the reattachment pressure peak at $s = 0.07$ m shifted by 0.003 m between the two finer grids. The value of the peak pressure remains almost identical for all three grids.

Figure 6 shows the data obtained using grids with a varying number of points in the wall-normal direction and identical normal spacing at the wall. The location of the peak pressure and C_f on the flare shifts downstream by 0.005 m when the number of wall-normal grid points is increased from 400 to 500. Their locations do not change appreciably when the grid size is increased further to 600 points. The peak values of pressure and C_f vary less than 2% for the two finer grids. The flow solutions upstream of the corner, including the separation point location, are almost identical for the 1000×500 and 1000×600 cases.

The data computed using successively higher numbers of wall-parallel grid points are presented in Fig. 7. The location of peak pressure and C_f shifts slightly downstream with the first refinement

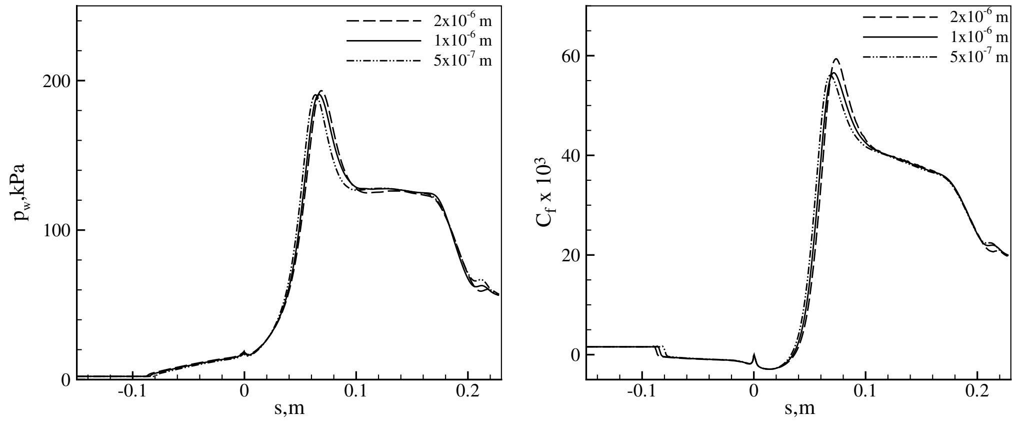

a) b)

Fig. 5 Effect of varying wall-normal spacing on computed a) wall pressure and b) skin-friction coefficient, using modified *k*-*ω* model for 36° flare at Mach 13.1.

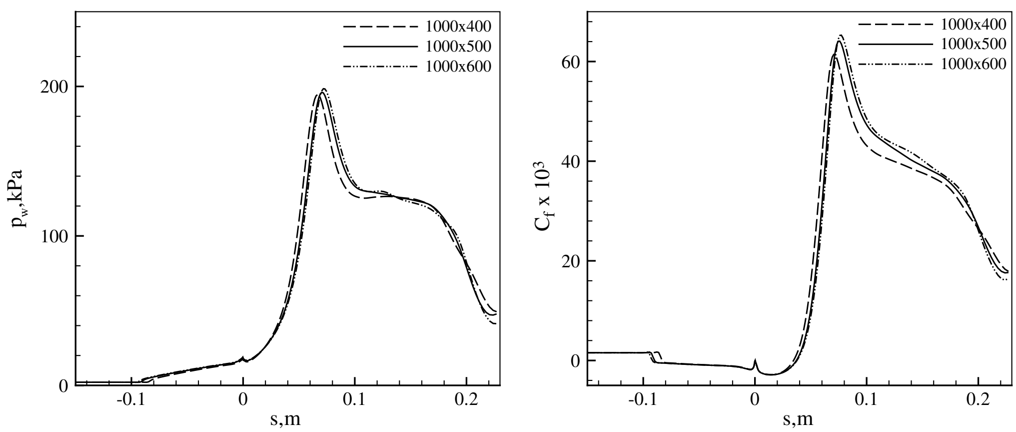

a) b)

Fig. 6 Effect of varying number of wall-normal grid points on computed a) wall pressure and b) skin-friction coefficient, using modified *k*-*ω* model for 36° flare at Mach 13.1.

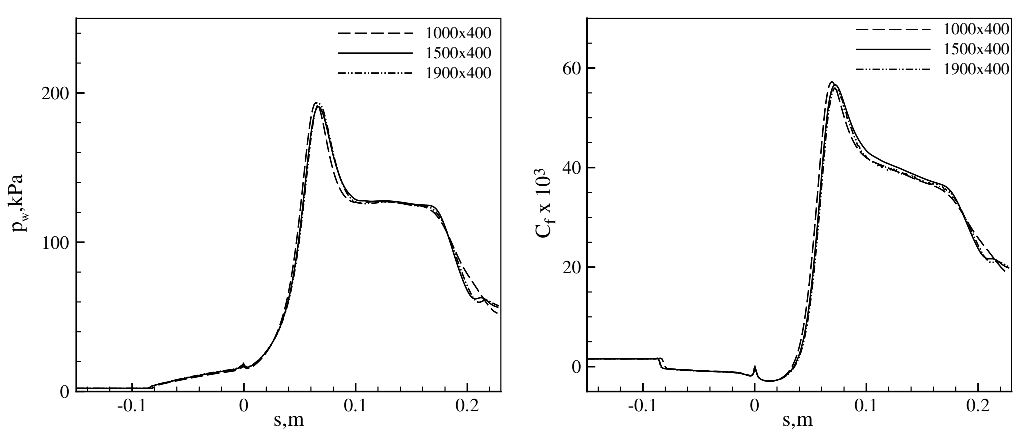

a) b)

Fig. 7 Effect of varying wall-parallel grid points on computed a) wall pressure and b) skin-friction coefficient, using modified *k*-*ω* model for 36° flare at Mach 13.1.

from 1000 to 1500 points, but there are almost no visible differences when the grid is further refined to 1900 points. Thus, 1500 points in the wall-parallel direction and 500 points in the wall-normal direction are adequate for computations using the standard and modified *k*-*ω* turbulence models. However, it is found that *k*-*ω* simulations using fine grids like 1500×500 require very small time steps for integration, such that a steady-state solution cannot be obtained in a reasonable computational time. By comparison, simulations on the 1500×400 grid are more robust, and therefore selected for all the *k*-*ω* results presented below. Based on the data presented in Fig. 6, using 400 points in the wall-normal direction will result in a slightly higher uncertainty: around 0.006 m in the location of the reattachment peak pressure and 7% in the peak skin-friction coefficient level, in the *k*-*ω* solutions. The wall-normal spacing at the wall is set at 1×10^{-6} m, which is equivalent to a y_2^+ value of 0.03 on the cone and less than 1.2 on the flare.

IV. Simulation Results

In this section, numerical solutions for the four test cases are presented in decreasing order of the strength of the shock/boundary-layer interaction (see Table 2). Initially, the standard Spalart–Allmaras and k-ω models are used in the computation. The shock-unsteadiness correction is then applied to show improvement in results over the standard models. The flow physics details are emphasized, and the computed wall pressure in the interaction region is compared with the experimental measurements.

The results presented below are computed on a 600×500 grid for the standard and modified Spalart–Allmaras models, and on a 1500×400 grid for the standard and modified k-ω models. These grids are chosen (Sec. III.C) based on a detailed grid refinement study for the 36° flare at Mach 13. The other three test cases are either at a lower Mach number, a lower flare angle, or both. The shock/boundary-layer interaction is therefore strongest for the first case, and the grid refinement study for this flow is expected to be sufficient for the other three flows.

The flowfield variables are initialized to freestream values over the entire domain, and the solution is advanced in time to reach a steady state. CFL numbers up to 1500 are used in computations using the standard and modified Spalart–Allmaras models. A maximum CFL of 50 is used for the standard and modified k-ω models. All the simulations are run in parallel using 16 CPU cores of a 2.66 GHz Intel processor-based machine. It takes approximately 92 CPU hours to reach steady-state solution using the Spalart–Allmaras model and about 625 CPU hours for the k-ω model.

A. 36 Degree Flare at Mach 13.1

The experimental schlieren image corresponding to the 36° flare at Mach 13.1 is shown in Fig. 8a. The boundary layer on the cone is marked by mild density variation and is identified in the figure. The boundary layer separates at the cone–flare junction, and a separation shock is located upstream of the corner. The separation shock is not clearly visible inside the cone boundary layer, but a distinct separation shock is observed outside the boundary layer. It is followed by a steeper shock on the flare downstream of reattachment. The clarity of the schlieren image is limited in the reattachment region, but distortions in the flare shock can be clearly seen. The flowfield exhibits some degree of unsteadiness, and the schlieren image corresponds to a single time realization of the unsteady flowfield. The oblique shock generated at the tip of the cone intersects the flare shock at the top right corner of the visualization window. The details of this shock–shock interaction are described below.

The numerical solution obtained using the standard Spalart–Allmaras turbulence model is presented in Fig. 8b. The normalized density contours plotted in the figure show the interaction of the cone shock and the flare shock clearly. The resulting shock–shock interaction generates a third shock and a free shear layer. Also, an expansion fan emanates from the triple point, and it reflects off the flare surface. The flow features generated by the intersection of the

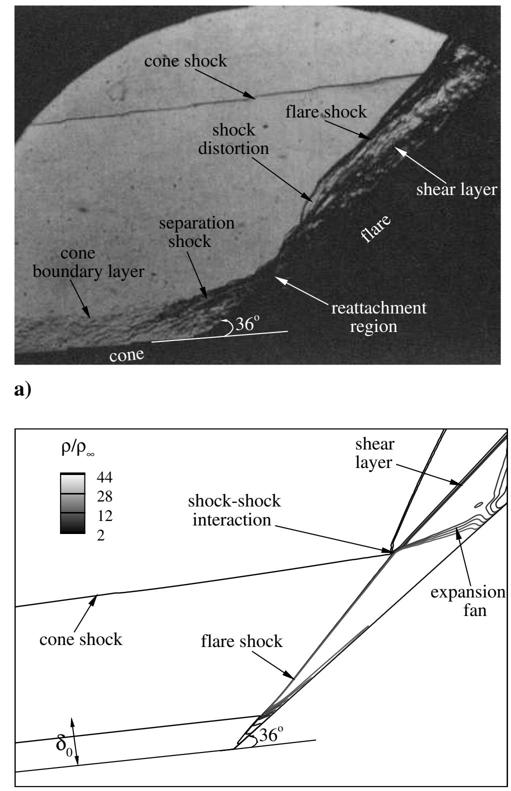

Fig. 8 Shock wave/boundary-layer interaction on a 36° flare at Mach 13.1: a) experimental schlieren image [12] and b) computed density contours using standard Spalart–Allmaras model.

cone and flare shocks are reproduced well by the numerical simulation, and they match the experimental schlieren image qualitatively. On the other hand, the computational solution differs markedly from the schlieren image at the cone–flare junction. The shock/boundary-layer interaction in this region and the underlying flow physics are the main focus of this work. The numerical solution predicts an oblique shock at the corner as opposed to a separation shock observed in the experiment. This is because the incoming boundary layer in the simulation does not separate upstream of the corner.

The difference in the flow topology between the experimental image and the computed solution results in a large mismatch between the corresponding surface pressure distributions plotted in Fig. 9. The numerical solution with a single attached shock results in a

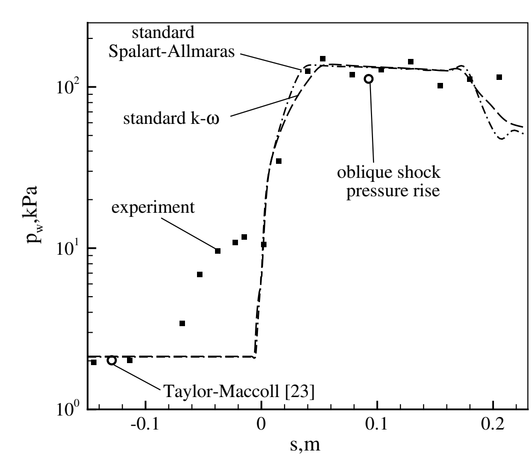

Fig. 9 Comparison of computed wall pressure with experiments [12] for 36° flare at Mach 13.1. Standard Spalart–Allmaras and standard k-ω models are used in the simulations.

Table 2 Shock/boundary-layer interaction characteristics for the cone–flare configuration[a]

	36° flare		30° flare	
	Mach 13	Mach 11	Mach 13	Mach 11
Mach number at incoming boundary-layer edge	10.37	9.1	10.27	9.1
Mach number normal to oblique shock M_{1n}	6.75	5.94	5.72	5.08
Inviscid pressure rise at corner p_2/p_1	56.0	43.4	40.0	31.7

[a]Subscripts 1 and 2 correspond to inviscid conditions upstream and downstream of an assumed oblique shock at the cone–flare junction.

distinct jump in pressure at the corner ($s \simeq 0$). On the other hand, the experimental data show a pressure rise upstream of the corner (at $s \simeq -0.08$ m). This pressure rise corresponds to the separation shock and is followed by a pressure plateau in the separation bubble. A further rise in the surface pressure downstream of the corner is due to flow reattachment on to the flare surface. Both the experimental data and the computed pressure on the cone are found to match the theoretical estimate of Taylor and Maccoll [23] upstream of the interaction region. Downstream of the reattachment, the simulation results compare well with measurements on the flare wall, but they overpredict the theoretical pressure rise obtained using oblique shock relations. The simulations predict a drop in surface pressure at the location $s \simeq 0.16$ m, where the expansion fan from the shock–shock interaction reflects from the flare wall.

Note that the wall pressure is plotted on a log scale in Fig. 9 to emphasize its variation in the vicinity of the separation point. In the absence of direct measurement of the separation location, it is estimated from an extrapolation of the initial pressure rise on the cone. As pointed out earlier, predicting the location of flow separation accurately is crucial to obtain the correct shock structure and flow topology in the interaction region.

The pressure data computed using the standard k-ω model are also presented in Fig. 9, and they match the results obtained using the Spalart–Allmaras turbulence model closely. The flowfield structure obtained using the k-ω model is also similar to the one presented in

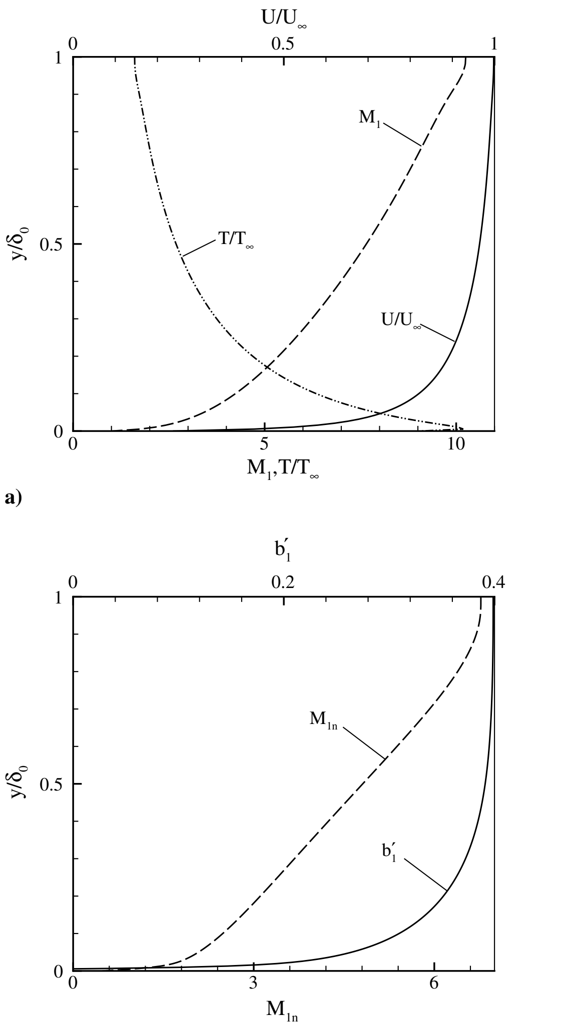

Fig. 10 10 Distribution of flow properties in the undisturbed boundary layer upstream of the shock/boundary-layer interaction region: a) Mach number M_1, normalized velocity U/U_∞, and normalized temperature T/T_∞; and b) shock-normal Mach number M_{1n} and shock-unsteadiness model parameter b_1'.

Fig. 8b. Both models fail to predict flow separation at the cone–flare junction, and therefore result in a significant disparity with the experimental shock structure and pressure data in this region. We attempt to improve the model predictions using the shock-unsteadiness correction proposed by Sinha et al. [8].

1. Application of the Shock-Unsteadiness Modification

The shock-unsteadiness correction is a function of the shock-normal Mach number upstream of the shock wave. This is calculated by

$$M_{1n} = \frac{\mathbf{u_1} \cdot \nabla p}{a_1 |\nabla p|} \tag{9}$$

Here, $\mathbf{u_1}$ and a_1 are the velocity vector and the speed of sound upstream of the shock wave, and ∇p is the pressure gradient at the shock.

The velocity and temperature values in the incoming boundary layer are plotted as a function of the wall-normal distance in Fig. 10a. The resulting distribution of the upstream Mach number is also shown in the figure. The shock wave generated at the cone–flare junction is plotted in terms of the normalized pressure contours in Fig. 11. The scale of the figure is magnified to highlight the incoming boundary layer on the cone. The value of M_{1n} along the shock is thus calculated using the upstream values along the local streamlines. The upstream Mach number varies between subsonic values near the wall to about 10 at the boundary-layer edge. The component of the upstream Mach number normal to the shock varies between 1.0 to 6.67 (see Fig. 10b). The shock-unsteadiness parameter b_1' computed using these values of M_{1n} is also plotted in the figure. It approaches zero in the near-wall region and attains a limiting value of 0.4 at the boundary-layer edge. For the Spalart–Allmaras model, the shock-unsteadiness parameter c_{b_1}' is evaluated using Eq. (8). It varies between 0.42 near the wall to -0.79 at the boundary-layer edge. In the following, the shock-unsteadiness correction is applied by using an average value of $c_{b_1}' = -0.32$ and $b_1' = 0.32$ for the Spalart–Allmaras and k-ω models, respectively. The average is calculated over a set of points distributed uniformly along the shock wave in the region where it overlaps with the incoming boundary layer. The solution obtained by implementing a detailed variation of the shock-unsteadiness parameter is discussed subsequently.

The function f_s identifies the shock waves and high compression regions in the flow in terms of the mean dilatation S_{ii}. These regions are highlighted in the modified k-ω solution in Fig. 12a. The near-wall region of the turbulent boundary layer also has nonzero S_{ii}, but care is taken to make f_s negligible in boundary-layer flows, where the standard model predictions are well validated. Figure 12b shows the distribution of f_s in the interaction region, and it captures the shock waves correctly. Depending on the level of compression, it smoothly varies between 0 and 1, where $f_s = 0$ corresponds to the standard model.

2. Modified Turbulence Model Predictions

The shock-unsteadiness corrected Spalart–Allmaras model with a negative c_{b_1}' results in a decrease of the turbulent kinematic eddy

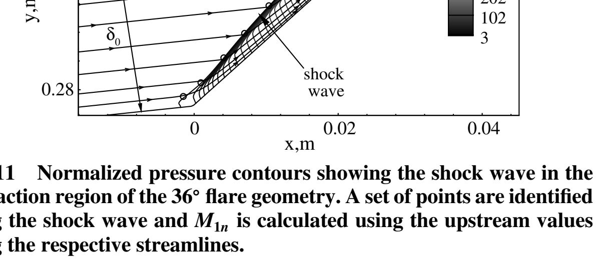

Fig. 11 Normalized pressure contours showing the shock wave in the interaction region of the 36° flare geometry. A set of points are identified along the shock wave and M_{1n} is calculated using the upstream values along the respective streamlines.

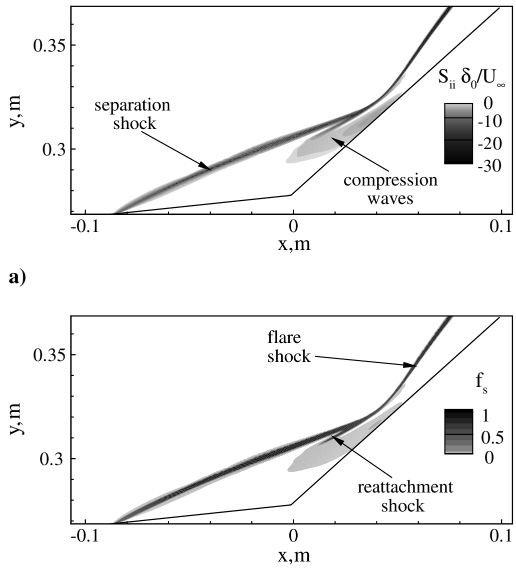

Fig. 12 Variation of a) normalized mean dilatation S_{ii} and b) shock-identifying function f_s showing different shocks and compression waves in the shock/boundary-layer interaction region.

viscosity at the shock wave. Lower levels of turbulence lead to an earlier separation of the boundary layer on the cone. The separation bubble in the numerical solution is identified in terms of a few characteristic streamlines in Fig. 13a, and the separation and reattachment points are marked by S and R, respectively. A separation shock is formed as the incoming boundary layer is deflected over the separation bubble. As the flow over the bubble reattaches the flare surface, a series of compression waves are generated. The resulting reattachment shock intersects the separation shock close to the flare surface (see magnified view in Fig. 13b) and forms an Edney type VI shock–shock interaction [24]. The flow pattern in the interaction region is shown schematically in Fig. 14. An oblique shock is generated at the triple point, and an expansion fan propagates toward the flare wall. The flow pattern is similar to that obtained in the shock–shock interaction further downstream on the flare, but the scale is smaller due to its proximity to the solid boundary. The shear layer generated at the triple point travels parallel to the flare surface and is marked by density contours in Fig. 13c. Also, a small secondary separation bubble formed at the corner is shown in the inset.

The density contours in Fig. 13c have strong resemblance with the experimental schlieren image in Fig. 8a. The density gradient in the upstream boundary layer is marked by contour lines of the time-averaged density parallel to the cone surface. In the vicinity of the separation point (S), the boundary-layer density variation overlaps with the separation shock contour lines. A similar effect is seen in the experimental schlieren image, and the separation shock is not distinctly visible inside the cone boundary layer. The density contours clearly mark the separation shock outside the boundary layer, and a small reattachment shock is visible on the flare. The reattachment shock cannot be discerned in the schlieren image, but the overall shock structure near the reattachment location matches the computed shock–shock interaction pattern closely. The flare shock generated at the triple point goes on to intersect the cone shock further downstream. The dark band in Fig. 8a along the flare wall downstream of reattachment is probably the free shear layer marked in the numerical solution. As expected, the flare shock in the RANS solution is steady, whereas distortions of the flare shock are visible in the experiment. These shock distortions appear to reduce significantly before the flare shock intersects the oblique shock from the cone tip.

The pressure data obtained using the shock-unsteadiness corrected Spalart–Allmaras model are shown in Fig. 15a. Comparison with the standard Spalart–Allmaras model results show two marked

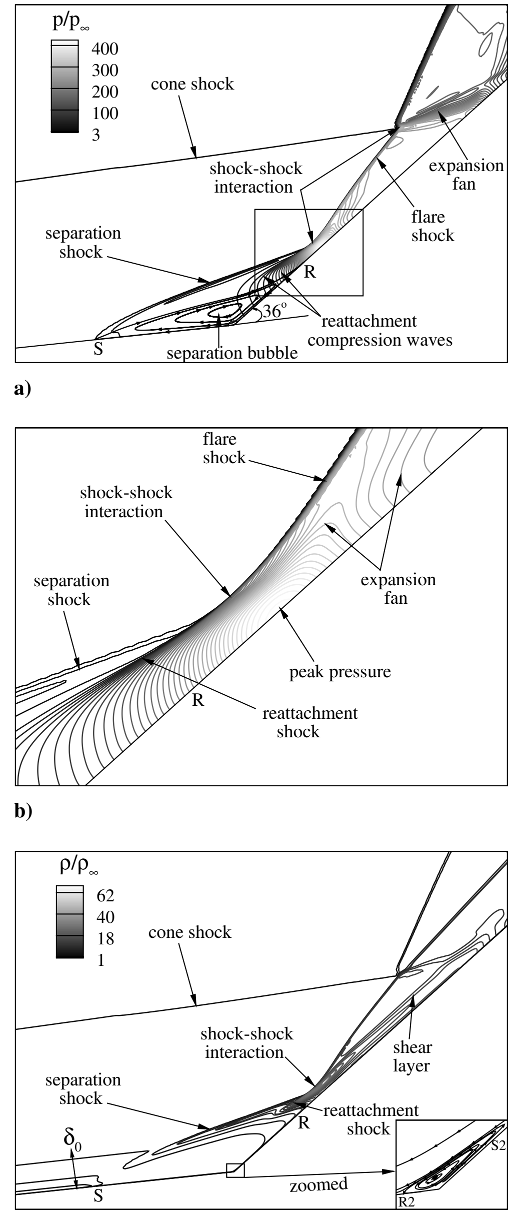

Fig. 13 Computed flow pattern using shock-unsteadiness modified Spalart–Allmaras model for 36° flare at Mach 13.1: a) normalized pressure contours, b) magnified view of the reattachment region, and c) normalized density contours.

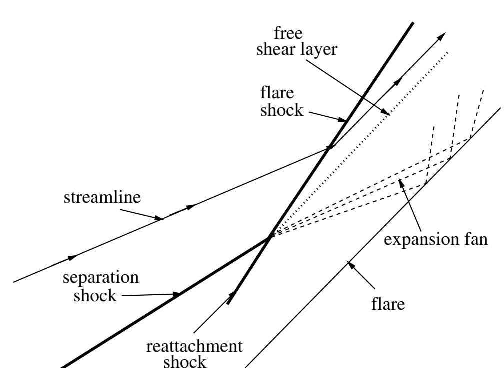

Fig. 14 Schematic sketch of Edney type VI shock–shock interaction [24].

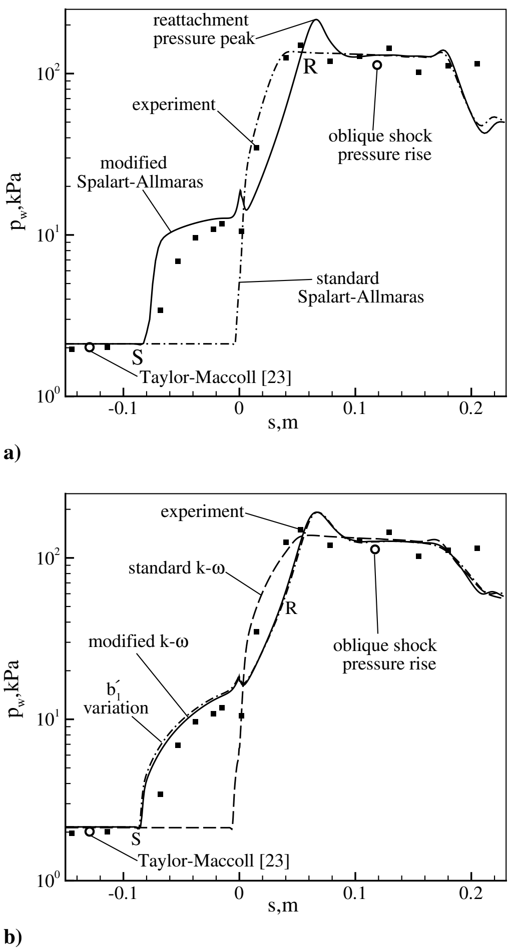

Fig. 15 Computed wall pressure is compared with experiments [12] for 36° flare at Mach 13.1. Shock-unsteadiness correction applied to a) Spalart–Allmaras model and b) *k*-ω model.

differences. First, the single pressure rise at the corner is replaced by a pressure rise due to the separation shock at $s = -0.08$ m followed by a pressure plateau and another pressure rise at the reattachment point on the flare. A sharp peak at $s = 0$ is due to a small secondary separation bubble formed at the corner (see Fig. 13c). Second, there is a local pressure peak immediately downstream of the reattachment point. This is caused by the shock–shock interaction in this region. The flow over the separation bubble gets overcompressed on passing through the separation and reattachment shock/compression waves. The pressure reaches a local maximum and then reduces when the expansion fan from the triple point reflects off the flare surface. There is indication of a local pressure peak in the experimental data, but the location of the peak and the reattachment pressure rise is somewhat upstream of the numerical prediction. The simulation also yields a slightly earlier separation than the experimental measurement. The locations of initial pressure rise on the cone, as obtained from experiment and computation, are listed in Table 3. The separation-bubble size, as estimated by the separation shock pressure rise and the reattachment pressure peak, is overpredicted by the modified Spalart–Allmaras model.

The modified *k*-ω model shows similar improvement over the standard *k*-ω model (see Fig. 15b). The shock-unsteadiness correction damps the TKE at the shock, and therefore results in a sizable recirculation bubble at the cone–flare junction. The separation shock pressure rise is located somewhat upstream of the experiment. Also, the reattachment pressure rise and the local pressure peak on the flare are downstream of the experimental data. The flowfield in the interaction region, including the separation bubble and the shock–shock interaction past reattachment, are very similar to that obtained using the modified Spalart–Allmaras model (Fig. 13). On the whole, the shock-unsteadiness correction, irrespective of the base turbulence model, reproduces the separation bubble at the cone–flare junction and the shock/expansion wave topology in the interaction region correctly. In spite of differences with the experimental data, the shock-unsteadiness corrected models yield significant improvement (see Table 3) in the surface pressure prediction over the standard Spalart–Allmaras and *k*-ω turbulence models.

As discussed earlier, the shock-unsteadiness parameter b_1' is a function of the local upstream Mach number normal to the shock, and its variation across the incoming boundary layer is plotted in Fig. 10b. A simulation is performed by considering the detailed variation of b_1' along the separation shock. The computed surface pressure, presented in Fig. 15b, is found to match the results obtained using an average value of the shock-unsteadiness parameter.

Table 3 Experimental and computed separation shock locations

	36° flare		30° flare	
	Mach 13	Mach 11	Mach 13	Mach 11
Experiment, mm	−80.1	−71.3	−37.8	——
Standard *k*-ω model, mm	−6.2	−7.5	−3.7	−3.7
Standard Spalart–Allmaras model, mm	−5.2	−6.5	−3.6	−3.6
Modified *k*-ω model, mm	−86.3	−86.1	−15.3	−15.0
Modified Spalart–Allmaras model, mm	−84.1	−83.9	−4.1	−4.0

B. 36 Degree Flare at Mach 10.97

Next, we consider the shock/boundary-layer interaction on a 36° flare at Mach 10.97. A lower freestream Mach number compared with the first test case leads to a lower boundary-layer edge Mach number on the cone, upstream of the interaction. The inviscid pressure rise assuming a single oblique shock at the corner and the corresponding Mach number normal to the shock wave are appreciably lower than the earlier case (see Table 2). This is expected to result in a weaker shock/boundary-layer interaction at the cone–flare junction. The strength of the interaction directly influences the extent of flow separation at the corner. The separation point in the experiment, as indicated by the location of initial pressure rise on the cone (see Table 3), is downstream in the Mach 11 flow than in the higher Mach number case. On the other hand, the Mach 13 flow is found to have a relatively colder wall ($T_w/T_{aw} = 0.15$) than the current test case ($T_w/T_{aw} = 0.17$). A colder wall with smaller values of T_w/T_{aw} increases the local Reynolds number, and hence reduces the separation-bubble size. Also, a lower unit Reynolds number in this flow (Table 1) compared with the earlier test case tends to increase the size of the separation bubble. The Reynolds number and cold wall effects counteract the trend observed due to the variation in Mach number in the later case, but they are found to have a minor effect on the shock/boundary-layer interaction. Overall, the second configuration results in a weaker interaction, in terms of a smaller separation bubble at the corner and a lower peak pressure at reattachment, than the first case.

The computed solution, in terms of the normalized pressure contours, is compared with the experimental schlieren image in Fig. 16. The simulation results correspond to the standard and modified *k*-ω turbulence models. The results obtained using the Spalart–Allmaras turbulence model are almost identical, and therefore not presented. The trends observed in this flow are very similar to those in the higher Mach number case presented earlier. The standard *k*-ω model suppresses flow separation, leading to a single oblique shock at the cone–flare junction. The solution does not match the experimental flow topology in this region. The shock-unsteadiness correction, by comparison, predicts a recirculation bubble at the corner. The flow topology is identical to that in Fig. 13, and it matches the shock structure observed in the schlieren image (Fig. 16a). Note that the corrugations in the flare shock are relatively weaker in this flow than the previous case (Fig. 8a), possibly due to the reduced strength of the shock/boundary-layer interaction.

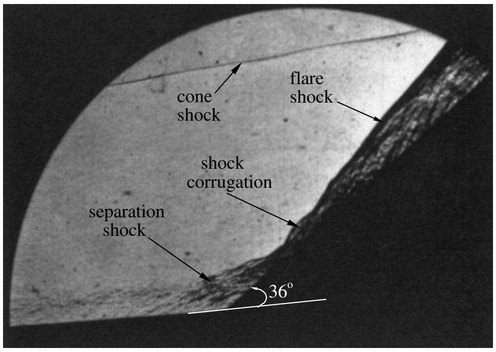

a)

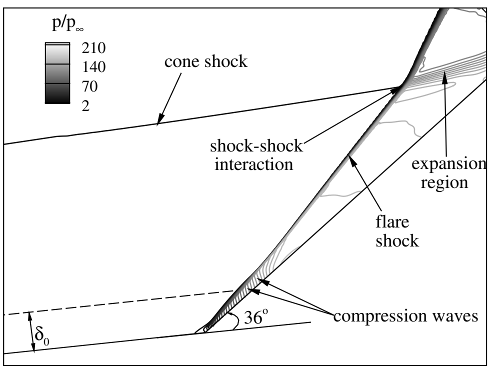

b)

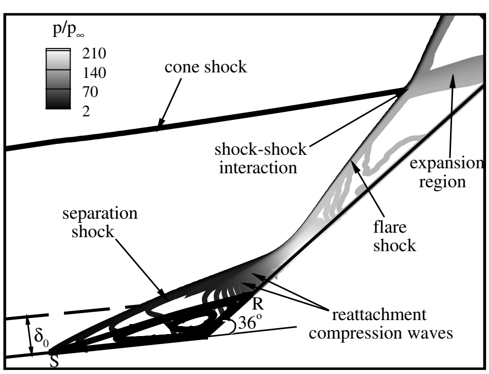

c)

Fig. 16 Shock wave/boundary-layer interaction on a 36° flare at Mach 10.97: a) experimental schlieren image [12], and computed normalized pressure contours using b) the standard *k*-*ω* model and c) the shock-unsteadiness modified *k*-*ω* model.

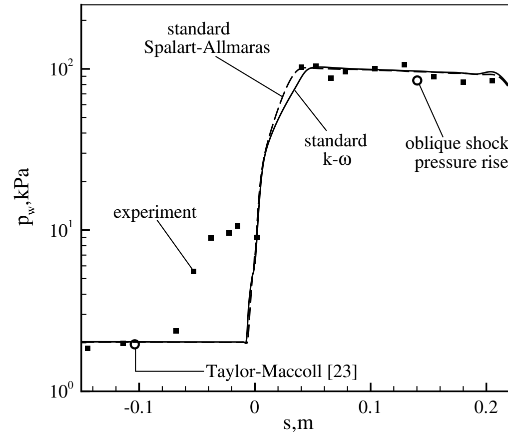

a)

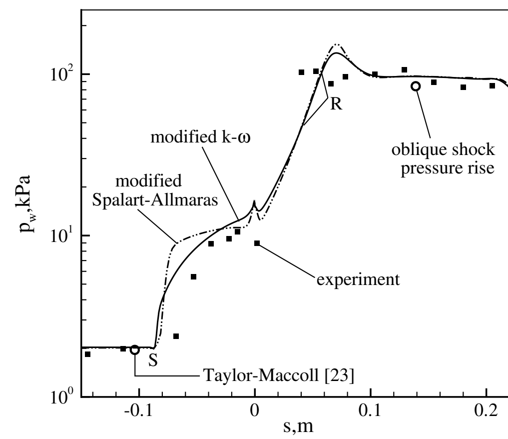

b)

Fig. 17 Comparison of computed wall pressure using a) standard and b) shock-unsteadiness modified turbulence models with experimental measurements [12] for 36° flare at Mach 10.97.

The surface pressure computed using the standard k-ω and Spalart–Allmaras turbulence models match the experimental and theoretical values on the cone (see Fig. 17a). The attached shock at the corner results in a single pressure jump at $s = 0$ to reach a uniform pressure on the flare. The computed pressure on the flare is comparable with the experimental measurements. There is a small dip in surface pressure toward the end of the flare, where the expansion fan from the second shock–shock interaction hits the wall.

The shock-unsteadiness correction (see Fig. 17b) yields an increase in the pressure at the separation point upstream of the corner. The separation locations for the two turbulence models are almost identical. The separation bubble is marked by a pressure plateau, followed by a further rise in pressure at reattachment. Similar to the earlier case, a local pressure peak is observed in the reattachment region due to the interaction between the separation and reattachment shock waves. The separation point identified in terms of the location of initial pressure rise on the cone is listed in Table 3. The shock-unsteadiness corrected turbulence models predict a separation point that is upstream of the experimental location. The experimental data also appear to indicate a steeper pressure rise at reattachment. An earlier separation and a later reattachment in the computation yield a larger separation bubble than the experiment. The simulations, however, reproduce the pressure plateau level in the recirculation region. This indicates that the inclination of the free shear layer enclosing the recirculation bubble is predicted correctly.

The implementation of the shock-unsteadiness correction in this flow follows the same procedure as outlined in the earlier case (Sec. IV.A). The upstream Mach number normal to the shock varies from the sonic value near the wall to about 6 at the edge of the boundary layer. The corresponding variation in b_1' is in the range 0 to 0.4. An average value of $b_1' = 0.31$ is used for this case. This results in the damping of the TKE at the shock, which promotes flow separation at the cone–flare junction. The parameter c_{b_1}' varies between 0.4 near the wall to -0.79 at the boundary-layer edge. Positive values of c_{b_1}' in the near-wall region promote turbulent eddy viscosity amplification, whereas negative values in the outer part of the boundary layer tend to suppress the turbulence. The overall effect due to average $c_{b_1}' = -0.3$ is to reduce the turbulence level compared with the standard Spalart–Allmaras model, and thus increase the size of the recirculation bubble at the cone–flare junction.

A comparison of the schlieren images in Figs. 8a and 16a shows that the cone shock is shifted outward at the lower Mach number. A lower postshock Mach number on the cone in the second case (Table 2) also results in a steeper flare shock for the same deflection at the corner. The shock–shock interaction point is downstream in the Mach 11 flow than in the Mach 13 case. The triple point is placed outside the visualization window at the lower Mach number (Fig. 16a), whereas it is located at the top right corner of the visualization window for the Mach 13 case. The numerical solutions show the same effect. The cone shock and the flare shock intersect at $x = 0.09$ m in the Mach 13 flow (Fig. 13c), and the interaction point is shifted downstream to $x = 0.11$ m for the Mach 11 flow (Fig. 16c). Note that there is a negligible effect of flow separation at the cone–flare junction on the location of the flare shock and its interaction with the cone shock. The triple point locations obtained using the standard and modified turbulence models are therefore identical in Figs. 16b and 16c.

It is difficult to make a quantitative comparison of the triple point location between the numerical solutions and the experimental results due to the lack of scale information for the schlieren images. A qualitative comparison, however, can be made by matching the size of the interaction region in the pressure data and approximate location of the separation shock in the schlieren image. It appears that the cone shock is placed higher in the experiment than the numerical solution. This could be because of the nose bluntness effects. The 6° half-angle cone used in the experiments has a nose radius of 3.8 cm, which is about 1.3% of the model length. The computations neglect this small nose radius and assume a sharp nose for the cone–flare geometry. A rounded nose of the experimental model results in a detached shock at the cone tip, which may be shifted outward compared with the attached shock predicted by computation. The location of the shock–shock interaction will also be moved accordingly and can explain the discrepancy between the numerical solution and the experimental image. A difference in the location of the cone shock is not expected to alter the postshock conditions on the cone and the shock/boundary-layer interaction at the cone–flare junction, which is the main focus of the current study.

C. 30 Degree Flare at Mach 12.92

The next test case corresponds to the 30° flare at Mach 12.92. The inviscid pressure rise through a single oblique shock at the corner and the corresponding upstream normal Mach number (listed in Table 2) are slightly lower than those for the 36° flare at Mach 11. A higher flare angle, but a lower Mach number, in the previous case results in an inviscid shock strength slightly higher than the current flow. The shock/boundary-layer interaction in the current case is therefore expected to be slightly weaker than, but comparable with, the interaction on the 36° flare at Mach 10.97. The values of the unit Reynolds number and T_w/T_{aw} for this case (Table 1) are in the same range as the earlier test cases, and minor differences in their values may not alter the strength of the shock/boundary-layer interaction dramatically.

The experimental data for this flow show an interesting pattern. The schlieren image in Fig. 18a is similar to that in the earlier cases in terms of the separation shock and the triple point observed at reattachment. However, the pressure data show no distinct jump at the separation shock location (see Fig. 19). There is a gradual, but low, rise in surface pressure closer to the corner. This may be because

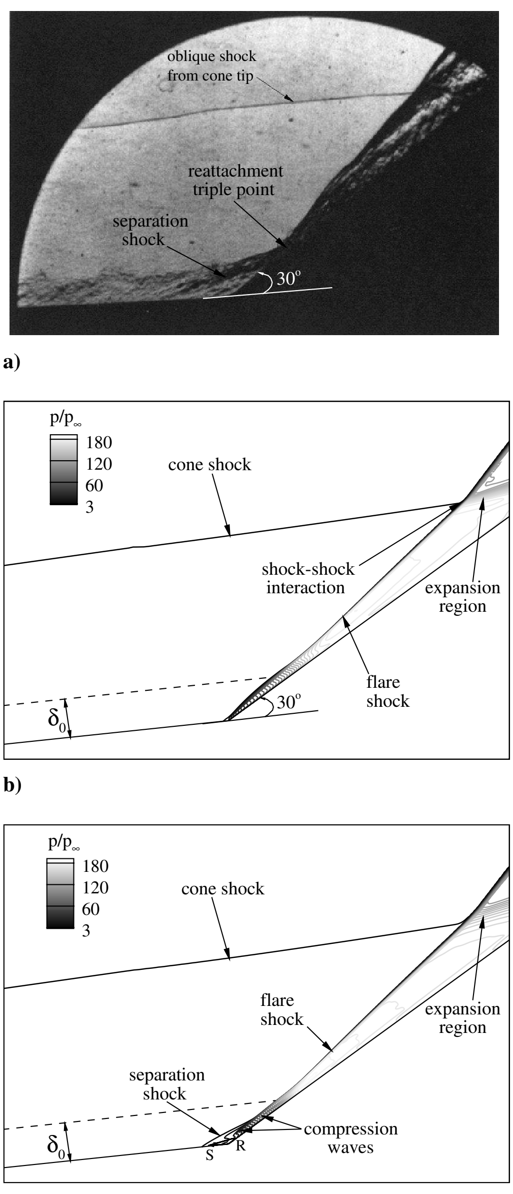

Fig. 18 Shock wave/boundary-layer interaction on a 30° flare at Mach 12.92: a) experimental schlieren image [12], and computed normalized pressure contours using b) standard *k*-*ω* model and c) modified *k*-*ω* model.

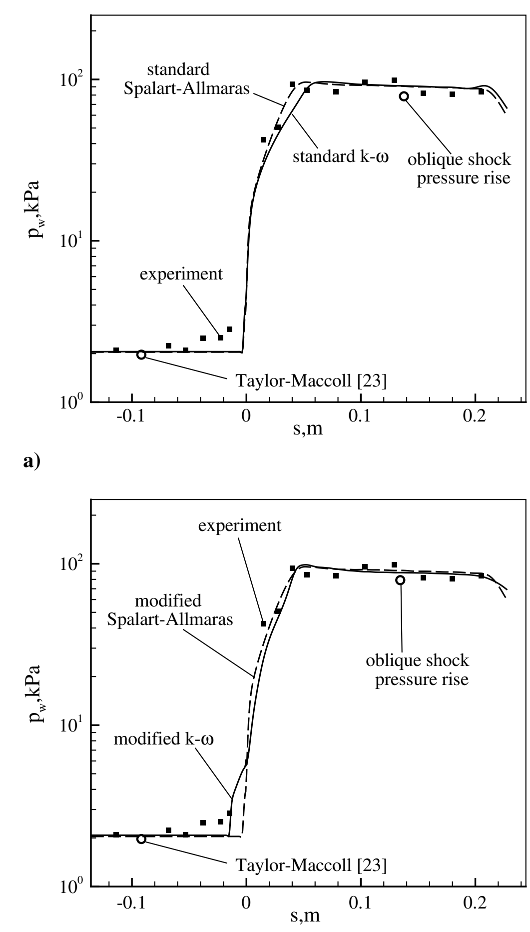

Fig. 19 Comparison of computed wall pressure using a) standard and b) shock-unsteadiness modified Spalart–Allmaras and *k*-*ω* turbulence models with experimental measurements [12] for 30° flare at Mach 12.92.

of large-scale unsteadiness of the corner flow. The shock/boundary-layer interaction may oscillate between a separated flow similar to that observed in the schlieren image and an attached flow without a recirculation bubble at the corner. The schlieren image is a single time realization of the flowfield, whereas the pressure data are representative of the mean flow and capture the time-averaged effect of any possible separation-bubble unsteadiness.

The RANS simulation yields a time-averaged flowfield solution. The standard Spalart–Allmaras and k-ω turbulence models predict an attached flow up to the corner (Fig. 18b), like the earlier cases. The surface pressure, presented in Fig. 19a, shows a similar trend. The shock-unsteadiness corrected Spalart–Allmaras model also predicts an attached flow at the junction and a single oblique shock on the flare. The solution is therefore identical to the standard Spalart–Allmaras model. The initial pressure is located slightly upstream of the corner ($s \simeq -0.004$ m) for both the models (see Table 3).

The shock-unsteadiness correction in the k-ω model, on the other hand, results in a small region of separated flow (see Fig. 18c). A separation shock wave can be seen in the figure, but the reattachment compression waves and their interaction with the separation shock are not clearly discernible because of the small scale of the interaction region. The pressure data obtained using the modified k-ω model (Fig. 19b) show a pressure rise upstream of the corner (at $s = -0.015$ m). A small pressure plateau and a slight overshoot in the surface pressure at reattachment can also be observed. The pressure variation in the interaction region is similar to that obtained in earlier cases, but it is smaller in scale. It does not match the pressure measurements in the separation bubble (-0.04 m $< s < 0$). The nonuniform variations in the experimental data in this region are probably due to the intermittent nature of the separation bubble. RANS methods, even with shock-unsteadiness correction, do not reproduce such intermittency effects.

D. 30 Degree Flare at Mach 10.98

The last test case corresponds to a 30° flare at Mach 10.98. Based on the pressure ratio and M_{1n} values presented in Table 2, it is the weakest of all the interactions considered in this work. The experimental schlieren image for this flow (Fig. 20a) shows a single oblique shock on the flare, with no indication of the flow separation at the corner. The pressure data on the cone (Fig. 21a) are uniform up to the cone–flare junction and are followed by a single pressure jump corresponding to the corner shock. This corroborates the fact that there is no boundary-layer separation in this case. This is reproduced well by both the standard and modified Spalart–Allmaras model computations. The computed density contours (Fig. 20b) match the schlieren image closely. The computed surface pressure also compares very well with the experimental measurements (Fig. 21a).

A magnified view of the pressure contours in the corner region (inset in Fig. 20b) shows the corner shock more clearly. The oblique shock is slightly curved in the region where there is a gradient in the upstream Mach number due to the incoming boundary layer on the cone. A turning of the low Mach number flow in the near-wall region onto the flare is achieved by a steeper shock compared with the outer part of the boundary layer, where a higher Mach number flow is deflected by the same angle through a more inclined shock wave. There is also a smaller pressure rise in the lower Mach number near-wall region, and a higher postshock pressure as the high Mach number flow is deflected in the outer part of the boundary layer. This variation in the surface pressure can be seen both in the experiment and computation (Fig. 21a). There is a sharp increase in pressure at the corner (from 2 to 13 kPa) followed by a gradual build up on the flare up to $s = 0.05$ m. Beyond this point, the uniform inviscid flow outside of the boundary layer (Mach number $= 9.03$) is deflected by 30°, and the flare pressure is close to the corresponding oblique shock value.

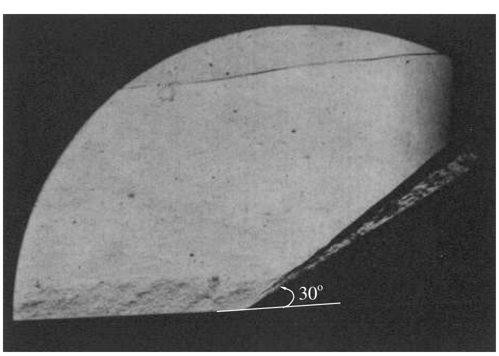

a)

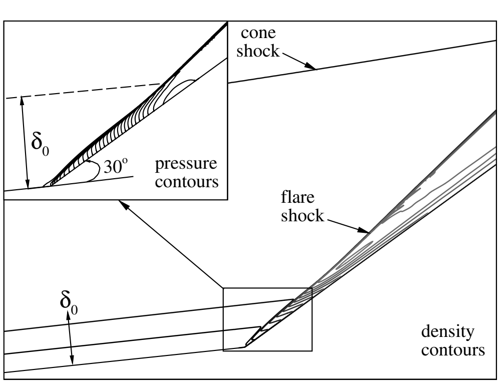

b)

Fig. 20 Shock wave boundary-layer interaction on a 30° flare at Mach 10.98: a) experimental schlieren image [12] and b) computed density and pressure field using standard Spalart–Allmaras model.

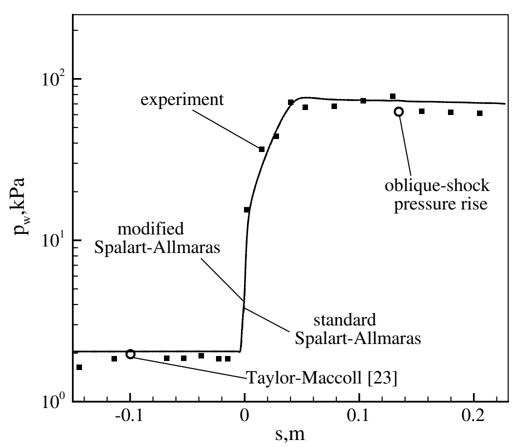

a)

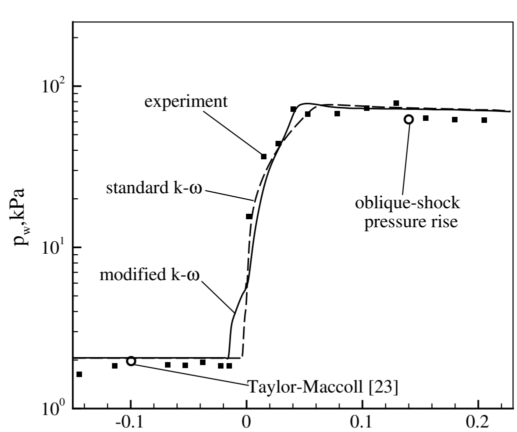

b)

Fig. 21 Shock-unsteadiness correction [10] applied to a) Spalart–Allmaras and b) k-ω turbulence models. Computed wall pressure is compared with experimental measurements [12] for 30° flare at Mach 10.98.

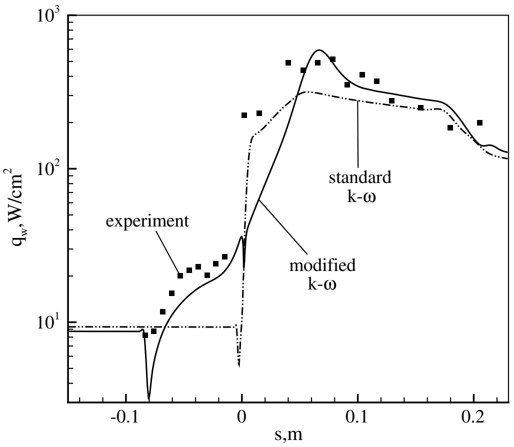

Fig. 22 Comparison of computed heat flux using standard and shock-unsteadiness modified *k-ω* turbulence models with experimental measurements [12] for 36° flare at Mach 13.1.

The standard k-ω model solution is identical to the Spalart–Allmaras model result presented in Fig. 20b. The shock-unsteadiness corrected k-ω model yields a small separation bubble at the corner. The pressure rise at the separation point located at $s = -0.015$ m, the pressure plateau in the recirculation zone, and a small overshoot in pressure at reattachment (see Fig. 21b) are similar to the previous case of 30° flare at Mach 12.92 (Fig. 19b). The shock structure in the interaction region is also similar to that observed at the higher Mach number (Fig. 18c), and it is not repeated here. The shock-unsteadiness correction in this flow is applied with an average value of $b_1' = 0.29$. The corresponding value of c_{b_1}' in the modified Spalart–Allmaras simulation is -0.26.

E. Heat-Flux Predictions

Figure 22 presents the surface heat flux computed using the standard and modified k-ω turbulence models for the strongest interaction case. The heat-flux variation follows a trend similar to that of the corresponding surface pressure data (see Fig. 15b). The standard model predicts a sharp rise in heat flux at the corner, whereas the shock-unsteadiness modification results in an elevated heating rate due to flow separation on the cone and a local peak at reattachment. Heat-flux prediction is thus closely related to the flow topology, and obtaining the separation bubble at the corner and the shock–shock interaction near reattachment results in significant improvement in heat-flux prediction. Nevertheless, there are noticeable differences between the computed and experimental data, and they are discussed below.

The shock-unsteadiness modification applied to the Spalart–Allmaras turbulence model leads to similar trends in heat-flux prediction, as in Fig. 22. However, the enhancement in heating rate due to flow separation and the peak heating at reattachment are lower than the modified k-ω predictions. Overall, the discrepancies with the experimental measurements are significantly larger than the k-ω model. The heat transfer results for the 36° flare at Mach 10.97 are qualitatively similar to that described above. For the remaining two cases with 30° flare, there are no major differences between the flow topologies computed using the standard and modified turbulence models (see Secs. IV.C and IV.D). The effect of the shock-unsteadiness modification on the surface heat flux is also quite small.

Note that all the computations show a dip in surface heat flux at a separation point (for example, at $s = -0.086$ m in Fig. 22) that is not observed in the experimental data. There are additional discrepancies between the measured and computed heating rates on the flare. Standard turbulence models like k-ϵ and k-ω show large errors in heat-flux predictions in shock-dominated hypersonic flows [2]. The recent k-ω model with stress limiter [3] also exhibits similar trends. As pointed out by Wilcox [3], this limitation is typical of all turbulence models that use Reynolds analogy and model the turbulent heat-flux vector in terms of a turbulent Prandtl number. This is true for the standard and modified turbulence models considered in this paper, and the error margin may be reduced by improving upon the constant turbulent Prandtl number assumption.

V. Conclusions

In this paper, hypersonic shock/turbulent boundary-layer interactions on cone–flare geometries are studied numerically. Four configurations with varying flare angles and freestream Mach numbers are simulated using the RANS methodology. The test cases range from strong interactions with large flow separation at the cone–flare junction to weak ones with attached flow at the corner. The standard Spalart–Allmaras and k-ω turbulence models suppress flow separation at the corner, and therefore do not reproduce the correct shock structure in the interaction region. This is probably due to a high level of turbulence predicted at the shock wave. By comparison, the shock-unsteadiness correction damps turbulence amplification at the shock. It reproduces the separation bubble observed experimentally, and it matches the surface pressure measurements well. The shock-unsteadiness corrected turbulence models also predict the flow topology in the interaction region, including the Edney type VI shock–shock interaction at reattachment, correctly. This results in appreciable improvement in the heat-flux predictions. The magnitude of correction decreases with the strength of the shock/boundary-layer interaction, such that it has a negligible effect for weak interactions, where the standard models perform reasonably well. Overall, the study highlights the implementation of the physics-based shock-unsteadiness correction in hypersonic flows and shows that this simple modification can yield significant improvement in flowfield prediction, irrespective of the baseline turbulence model.

Acknowledgment

The authors thank the Indian Space Research Organization for supporting this research under the Sponsored Research (RESPOND) program.

References

[1] Roy, C. J., and Blottner, F. G., "Review and Assessment of Turbulence Models for Hypersonic Flows," *Progress in Aerospace Sciences*, Vol. 42, Nos. 7–8, 2006, pp. 469–530. doi:10.1016/j.paerosci.2006.12.002

[2] Coakley, T. J., and Huang, P. G., "Turbulence Modeling for High Speed Flows," AIAA Paper 1992-0436, Jan. 1992.

[3] Wilcox, D. C., "Formulation of the k-ω Turbulence Model Revisited," *AIAA Journal*, Vol. 46, No. 11, 2008, pp. 2823–2838. doi:10.2514/1.36541

[4] Knight, D., Yan, H., Panaras, A. G., and Zheltovodov, A., "Advances in CFD Prediction of Shock Wave Turbulent Boundary Layer Interactions," *Progress in Aerospace Sciences*, Vol. 39, No. 2-3, 2003, pp. 121–184. doi:10.1016/S0376-0421(02)00069-6

[5] Horstman, C. C., "Prediction of Hypersonic Shock-Wave/Turbulent Boundary-Layer Flows," AIAA Paper 1987-1367, June 1987.

[6] Huang, P. G., and Coakley, T. J., "Turbulence Modeling for Complex Hypersonic Flows," AIAA Paper 1993-0200, Jan. 1993.

[7] Knight, D. D., and Degrez, G., "Shock Wave Turbulent Boundary Layer Interactions in High Mach Number Flows: A Critical Survey of Current Numerical Prediction Capabilities," AGARD Advisory Rept. 319, Vol. 2, 1998, pp. 1.1–1.35.

[8] Sinha, K., Mahesh, K., and Candler, G. V., "Modeling Shock-Unsteadiness in Shock/Turbulence Interaction," *Physics of Fluids*, Vol. 15, No. 8, 2003, pp. 2290–2297. doi:10.1063/1.1588306

[9] Mahesh, K., Lele, S. K., and Moin, P., "The Influence of Entropy Fluctuations on the Interaction of Turbulence with a Shock Wave," *Journal of Fluid Mechanics*, Vol. 334, 1997, pp. 353–379. doi:10.1017/S0022112097004576

[10] Sinha, K., Mahesh, K., and Candler, G. V., "Modeling the Effect of Shock-Unsteadiness in Shock/Turbulent Boundary-Layer Interactions," *AIAA Journal*, Vol. 43, No. 3, 2005, pp. 586–594. doi:10.2514/1.8611

[11] Pasha, A. A., and Sinha, K., "Shock-Unsteadiness Model Applied to Oblique Shock-Wave/Turbulent Boundary-Layer Interaction,"

International Journal of Computational Fluid Dynamics, Vol. 22, No. 8, 2008, pp. 569–582.
doi:10.1080/10618560802290284

[12] Holden, M. S., "Studies of the Mean and Unsteady Structure of Turbulent Boundary-Layer Separation in Hypersonic flow," AIAA Paper 1991-1778, June 1991.

[13] Sinha, K., "Shock-Unsteadiness Model Applied to Hypersonic Shock-Wave/Turbulent Boundary-Layer Interactions," AIAA Paper 2006-0126, 2006.

[14] Wilcox, D. C., *Turbulence Modeling for CFD*, 2nd ed., DCW Industries, La Cañada, CA, 2000, pp. 491–492.

[15] Spalart, P. R., and Allmaras, S. R., "A One-equation Turbulence Model for Aerodynamic Flows," AIAA Paper 1992-0439, Jan. 1992.

[16] Wilcox, D. C., "Reassessment of the Scale-Determining Equation for Advanced Turbulence Models," *AIAA Journal*, Vol. 26, No. 11, 1988, pp. 1299–1310.
doi:10.2514/3.10041

[17] Haidinger, F. A., and Friedrich, R., "Computation of Shock Wave Turbulent Boundary Layer Interactions Using a Two Equation Model with Compressibility Corrections," *Applied Scientific Research*, Vol. 51, Nos. 1–2, 1993, pp. 501–505.
doi:10.1007/BF01082582

[18] Menter, F. R., "Two-Equation Eddy-Viscosity Turbulence Models for Engineering Applications," *AIAA Journal*, Vol. 32, No. 8, 1994, pp. 1598–1605.
doi:10.2514/3.12149

[19] MacCormack, R. W., and Candler, G. V., "The Solution of the Navier–Stokes Equations Using Gauss–Siedel Line Relaxation," *Computers and Fluids*, Vol. 17, No. 1, 1989, pp. 135–150.
doi:10.1016/0045-7930(89)90012-1

[20] Sinha, K., and Candler, G. V., "Convergence Improvement of Two-Equation Turbulence Model Calculations," AIAA Paper 1998-2649, June 1998.

[21] Wright, M. J., Candler, G. V., and Bose, D., "Data-Parallel Line Relaxation Method for the Navier–Stokes Equations," *AIAA Journal*, Vol. 36, No. 9, 1998, pp. 1603–1609.
doi:10.2514/2.586

[22] Reddy, D. S. K., and Sinha, K., "Hypersonic Turbulent Flow Simulation of FIRE II Reentry Vehicle Afterbody," *Journal of Spacecraft and Rockets*, Vol. 46, No. 4, 2009, pp. 745–757.
doi:10.2514/1.41380

[23] Taylor, G. I., and Maccoll, J. W., "The Air Pressure on a Cone Moving at High Speed," *Proceedings of the Royal Society of London A*, Vol. 139, 1933, pp. 278–311.
doi:10.1098/rspa.1933.0017

[24] Edney, B. E., "Anomalous Heat Transfer and Pressure Distributions on Blunt Bodies at Hypersonic Speeds in the Presence of an Impinging Shock," Aeronautical Research Institute of Sweden, FFA Rept. 115, Stockholm, Feb. 1968.

R. Bowersox
Associate Editor